

Phase diagram of a two-dimensional system with anomalous liquid properties

Ahmad M. Al mudallal,¹ Sergey V. Buldyrev,² and Ivan Saika-Voivod¹

¹*Department of Physics and Physical Oceanography, Memorial University of Newfoundland, St. John's, Newfoundland A1B 3X7, Canada*

²*Department of Physics, Yeshiva University, 500W 185th Street, New York, New York 10033, USA*

(Received 30 March 2012; accepted 25 June 2012; published online 18 July 2012)

Using Monte Carlo simulation techniques, we calculate the phase diagram for a square-shoulder square-well potential in two dimensions that has been previously shown to exhibit liquid anomalies consistent with a metastable liquid-liquid critical point. We consider the liquid, gas, and five crystal phases, and find that all the melting lines are first order, despite a small range of metastability. One melting line exhibits a temperature maximum, as well as a pressure maximum that implies inverse melting over a small range in pressure. © 2012 American Institute of Physics. [<http://dx.doi.org/10.1063/1.4735093>]

I. INTRODUCTION

Core-softened potentials were first used by Stell, Hemmer and co-workers in a lattice gas system to discuss the isostructural solid-solid phase transition that ends in a second critical point.¹⁻³ Core-softened potentials were also used to study single-component systems in a liquid state, such as liquid metals.⁴⁻¹¹ They have been also used to study liquid anomalies in 1D¹²⁻¹⁴ and 2D.¹⁵⁻¹⁸ Calculations in Refs. 19 and 20 show that a core-softened potential can be considered as a realistic first-order approximation for the real interaction between water molecules resulting from averaging over the angular part.

Interest in the study of liquid-liquid (L-L) phase transitions in single-component systems grew dramatically after such a transition and accompanying critical point were proposed for water as an explanation for its anomalous properties.²¹ Various studies have been done to understand the L-L phase transition and associated phenomena. Some of these studies focussed on the “two-liquid” model to explain liquid properties.²²⁻²⁴ Other studies were based on using anisotropic potentials.^{25,26} Franzese *et al.* showed that the liquid-liquid phase transition and accompanying critical point can also arise from a shoulder-like potential with two characteristic distances (hard core and soft core).²⁷ In this work, the authors reported in 3D molecular dynamics (MD) simulations the existence of two liquid phases, the low-density liquid phase and the high-density liquid phase, and showed that these two phases can occur in the system with no density anomaly. On the other hand, 2D simulation studies reproduce the density anomaly but no second critical point.¹³ For a review of unusual behavior of isotropic potentials with two energy scales in 2D, see Ref. 28. In general, the phase behavior of 2D systems is richer, with crystallization able to proceed through a hexatic phase,²⁹ or even through a less well understood way when long-range repulsions are present.³⁰

Gibson and Wilding³¹ studied a family of ramp potentials¹⁶ for which the L-L critical point systematically moved from a stable position in the phase diagram to a

metastable one. Ryzhov and Stishov³² tracked the change of the L-L transition line as a function of the width of the shoulder in a square-shoulder potential. A fuller examination of the phase behavior of the square-shoulder potential^{33,34} placed the liquid anomalies in the context of the crystal phases and gave emphasis to the “quasi binary mixture” nature of the system at low temperature (which allows for an “amorphous gap” of increased liquid stability between crystal structures as a function of density). Lattice models have also played a role in gaining basic insight into the mechanism of the L-L transition and associated liquid-state anomalies,^{35,36} and are more amenable to analytic treatments.^{37,38}

Scala and co-workers¹⁸ carried out MD simulations in 2D of the square-shoulder square-well (SSSW) potential shown in Fig. 1 to study liquid anomalies. Buldyrev *et al.*³⁹ continued with the SSSW model in 2D and 3D in order to study liquid-liquid phase transitions. For the 2D system, they produced a phase diagram showing liquid anomalies in relation to approximate crystallization lines for a range in pressure P and temperature T near a potential L-L critical point. Their phase diagram shows the gas-liquid coexistence curve and crystallization lines for a low-density triangular (LDT) and higher density square crystal. It also shows the first critical point and the hypothetical position of the second critical point, which coincides with the crossing of the two crystallization lines. Thus, unavoidable crystallization renders the L-L critical point not directly observable, or obscured. Their crystallization lines were determined from examining the behavior of the pressure, structure, and dynamics along isochores. They are estimates of the limit of liquid stability, or rather the limit of metastability, with respect to the crystal, rather than thermodynamically determined coexistence lines. As the system is two-dimensional, the nature of the crystallization transition is also under question, in so far that in two dimensions, crystallization can proceed in a continuous way via a hexatic phase rather than through a first-order phase transition.

In the present work, we carry out free energy calculations, based primarily on Monte Carlo (MC) simulation, to

determine the coexistence conditions between the liquid and crystal phases for a wide range of P and T , including the smaller range presented in Ref. 39. In doing so, we find two low-density crystal phases not previously reported for the model. We find that all the transitions are at least weakly first order. The crystallization lines reported in Ref. 39 are below our calculated melting lines. Additionally, the square crystal shows a maximum temperature in its melting curve, as well as a maximum in pressure. Thus, the present model is a useful one for studying the rare phenomenon of inverse melting, in which the liquid may freeze to the crystal upon heating.

This paper is organized as follows. In Sec. II, we discuss all the free energy and computer simulation techniques used in carrying out this work. In Sec. III, we show our results. In Sec. IV we present a discussion and we give our conclusions in Sec. V.

II. METHODS

A. Model and simulations

The model we study is the step pair potential shown in Fig. 1. As we are carrying out our studies in two dimensions, the model describes disks with a hard-core diameter σ and an attractive well extending out to a radial distance of $c = \sqrt{3}\sigma$. The attractive well itself contains a shoulder, with a pair interaction energy of $-\epsilon/2$ for $\sigma < r < b$ and energy of $-\epsilon$ for $b < r < c$. The parameter b was originally chosen to be $\sqrt{2}\sigma$ so that there would exist a LDT phase and a higher density square (S) phase with the same potential energy per particle of -3ϵ , i.e., two energetically degenerate phases of well separated densities.³⁹ The idea behind this was to allow for distinct liquid states, one based on square packing and the other on the more open triangular packing, in analogy to what is thought to be the case for water. At high pressure the system ultimately must form the close-packed triangular phase (high-density tri-

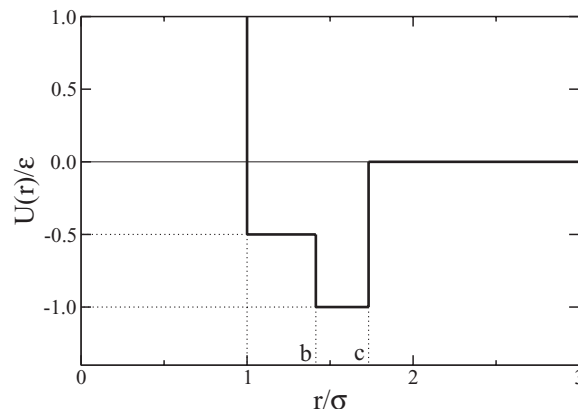


FIG. 1. The pair potential used in this study is an isotropic step potential with hard-core diameter σ . $b = \sqrt{2}\sigma$ is the soft-core distance, and $c = \sqrt{3}\sigma$ is the attractive distance limit. r is the distance between two particles and ϵ is the bond energy.

angular (HDT)), with potential energy per particle of -1.5ϵ . We find two additional crystals, phases A and Z, with per particle energies -3.25ϵ and -3.5ϵ , respectively. The various crystal phases are depicted in Fig. 2. Our goal is to calculate coexistence lines between the five crystal phases, the liquid (L) and the gas (G).

The liquid-state properties of the model were extensively studied in Ref. 39 using discrete MD simulation. The S and LDT crystallization lines were determined in that work from pressure isochores and from direct observation of crystal-like structural and dynamical behavior. Here, we calculate the crystal coexistence lines using free energy techniques that employ for the most part MC simulations performed at constant particle number N , P , and T , i.e., in the NPT ensemble.⁴⁰ Depending on the phase, the pressure is kept constant by changing the volume isotropically (for L, S, HDT, and LDT), by allowing rectangular dimensions of the simulation cell to change length independently while maintaining a right angle

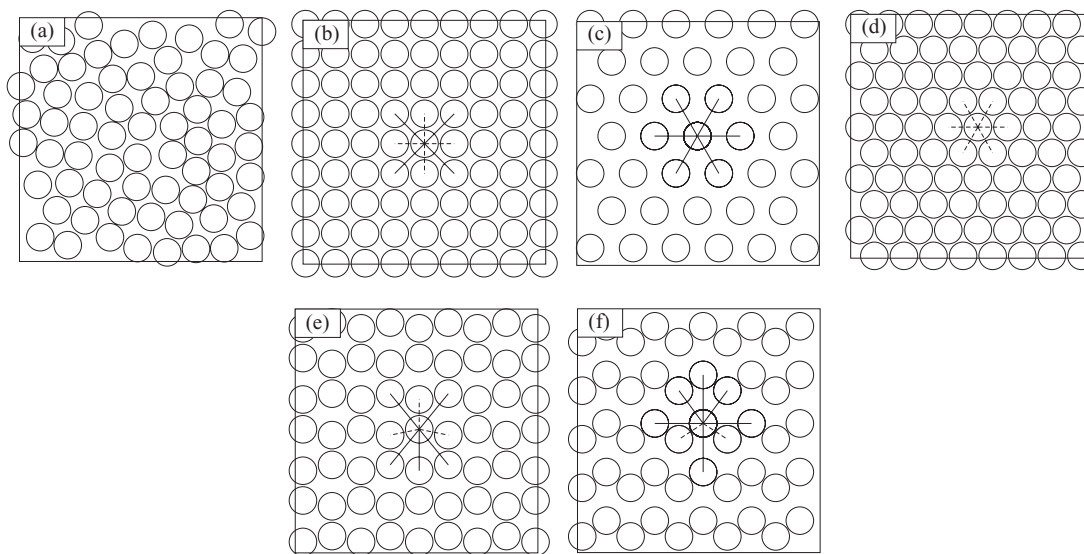


FIG. 2. Illustration of the phases modelled. (a) The liquid (L), here shown as a small portion of a simulation in which distinct local packing environments are visible. (b) The square crystal (S). (c) The low-density triangular crystal (LDT). (d) The high-density triangular crystal (HDT). (e) The A crystal. (f) The Z crystal. Line segments for the crystal phases indicate a bond with energy $-\epsilon$ and a dashed line segment one with energy $-\epsilon/2$.

(for A and Z), or by allowing the angle to change as well (as a check for all phases). The system sizes and box shapes are as follows: (L) $N = 1020$ and 986 , square box; (S) $N = 1024$ square box, and $N = 992$ with rectangular box $L_y = 32L_x/31$; (HDT and LDT) $N = 986$, $L_y = 17\sqrt{3}L_x/29$; (A) $N = 952$, $L_y = 28(\sin 12^\circ + 1)L_x/(34\cos 12^\circ)$ initially; (Z) $N = 968$, square box initially. The different box shapes (and hence number of particles) are used as consistency checks, and indeed we do not detect any difference in the results based on the particular choice used.

B. Solid-liquid and solid-solid coexistence

First-order transition lines can be determined using a method developed by Kofke to trace coexistence curves.^{41,42} Kofke refers to his method as Gibbs-Duhem integration, and it is based on the Clapeyron equation which describes the temperature dependence of the pressure at which two phases coexist

$$\frac{dP}{dT} = \frac{\Delta s}{\Delta v} = \frac{\Delta h}{T\Delta v}, \quad (1)$$

where Δs is the molar entropy difference, Δh is the molar enthalpy difference, and Δv is the molar volume difference between the two coexisting phases. Tracing the coexistence curve requires that one point on the coexistence curve be known and then the rest of the curve can be found by integration of Eq. (1), in particular using the enthalpy since it is much easier to calculate than the entropy. We carry out the integration using a second-order predictor-corrector method.^{43,44}

To obtain the first coexistence point between the liquid and the S crystal, we first determine the respective equations of state along an isotherm by carrying out several NPT simulations. We choose $k_B T/\epsilon = 0.55$ so that we are above the L-G critical temperature, where k_B is the Boltzmann constant. Once the equations of state are known, we calculate the chemical potential μ for each phase as a function of number density ρ by integrating the pressure via^{40,45}

$$\beta\mu(\rho) = \beta f(\rho^*) + \beta \int_{\rho^*}^{\rho} \frac{P(\rho')}{\rho'^2} d\rho' + \frac{\beta P}{\rho}, \quad (2)$$

where $\beta = (k_B T)^{-1}$ and f is the Helmholtz free energy per particle calculated at a reference number density ρ^* .

To carry out the integration, we fit the liquid isotherm to Eq. (3) and the solid isotherm to Eq. (4) (Refs. 47 and 46)

$$\beta P = \frac{\rho}{1 - a_l \rho} + b_l \left(\frac{\rho}{1 - a_l \rho} \right)^2 + c_l \left(\frac{\rho}{1 - a_l \rho} \right)^3, \quad (3)$$

$$\beta P = a_s \rho^2 + b_s \rho + c_s, \quad (4)$$

where $a_{l,s}$, $b_{l,s}$, and $c_{l,s}$ are the fit parameters. Integration of Eq. (3) from zero to a density of interest yields the chemical potential of liquid, as given in Eq. (5). Similarly, integration of Eq. (4) from a reference density to the density of interest

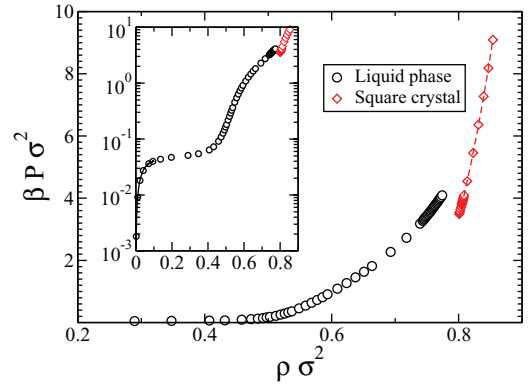


FIG. 3. Equations of state of the liquid (circles) and S crystal (diamonds) at $k_B T/\epsilon = 0.55$. The curves show fits according to Eqs. (3) and (4), with $a_l = -0.457818$, $b_l = -9.18372$, and $c_l = 33.4007$ for the liquid (inset) and $a_s = 479.035$, $b_s = -686.583$, and $c_s = 246.067$ for the crystal.

yields the chemical potential of solid, as given in Eq. (6),^{46,47}

$$\begin{aligned} \beta\mu_l(\rho) = & \ln \left(\frac{\rho \Lambda^2}{1 - a_l \rho} \right) + \frac{b_l/a_l - c_l/a_l^2 + 1}{1 - a_l \rho} \\ & + \frac{c_l/2a_l^2 + b_l \rho}{(1 - a_l \rho)^2} + \frac{c_l \rho^2}{(1 - a_l \rho)^3} \\ & - (b_l/a_l - c_l/2a_l^2 + 1), \end{aligned} \quad (5)$$

$$\begin{aligned} \beta\mu_s(\rho) = & 2a_s \rho + b_s [\ln(\rho) + 1] \\ & - [a_s \rho^* + b_s \ln(\rho^*) - c_s/\rho^*] \\ & + \beta f^{\text{ex}}(\rho^*) + \ln(\Lambda^2 \rho^*) - 1, \end{aligned} \quad (6)$$

where $\Lambda = h/\sqrt{(2\pi m k_B T)}$ is the de Broglie thermal wavelength, where it is assumed to equal unity since it plays no role in locating the coexistence pressure (along an isotherm). $f^{\text{ex}}(\rho^*)$ is the excess Helmholtz free energy per particle calculated at ρ^* .

For the liquid, Eq. (3) provides a good fit only up to $\rho \approx 0.1$, and so from $\rho = 0$ to $\rho_l^* = 0.09418$ we use Eq. (5), and then integrate Eq. (2) numerically, using different interpolation orders to estimate uncertainty. The equations of state for the liquid and the S crystal are shown in Fig. 3.

We calculate the crystal reference Helmholtz free energy using the Frenkel-Ladd method.⁴⁸ In this method, a harmonic potential is added to the original system to define a new system potential energy,

$$U_\lambda = U(\vec{r}^N) + \lambda \sum_{i=1}^N (\vec{r}_i - \vec{r}_{0,i})^2, \quad (7)$$

where \vec{r}_i is the position of particle i and $\vec{r}_{0,i}$ is its ideal lattice position, and $U(\vec{r}^N)$ is the unaltered system potential energy. U_λ is such that at coupling parameter $\lambda = 0$ the original model is recovered and for sufficiently large λ , the system behaves as an ideal Einstein crystal. A thermodynamic integration at a particular T and ρ is carried along λ to determine the Helmholtz free energy difference between the Einstein crystal and the original model. The excess free energy per particle for

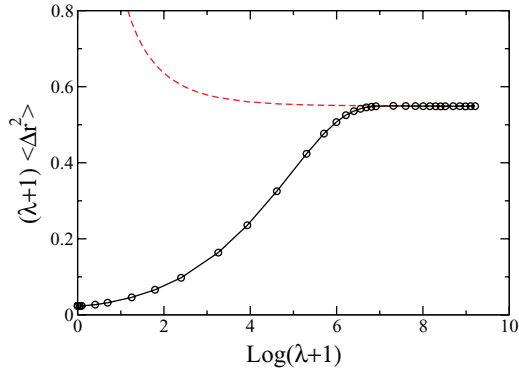


FIG. 4. The mean-squared displacement transformed by Eq. (12) as a function of coupling parameter λ calculated by computer simulation (solid curve is a guide to the eye). Dashed line is the theoretical value given by Eq. (10).

the model is then expressed as⁴⁰

$$\beta f^{\text{ex}} = \beta f_{\text{Ein}} + \frac{\beta \Delta F^{\text{CM}}}{N} + \frac{\ln(\rho^*)}{N} - \frac{d}{2N} \ln(N) - \frac{d}{2N} \ln\left(\frac{\beta \lambda_{\text{max}} m}{2\pi}\right) - \beta f^{\text{id}}, \quad (8)$$

where $d = 2$ is the dimensionality of the system and $m = 1$ is the mass of the particle. The first term in Eq. (8) represents the free energy of the ideal (non-interacting) Einstein crystal,

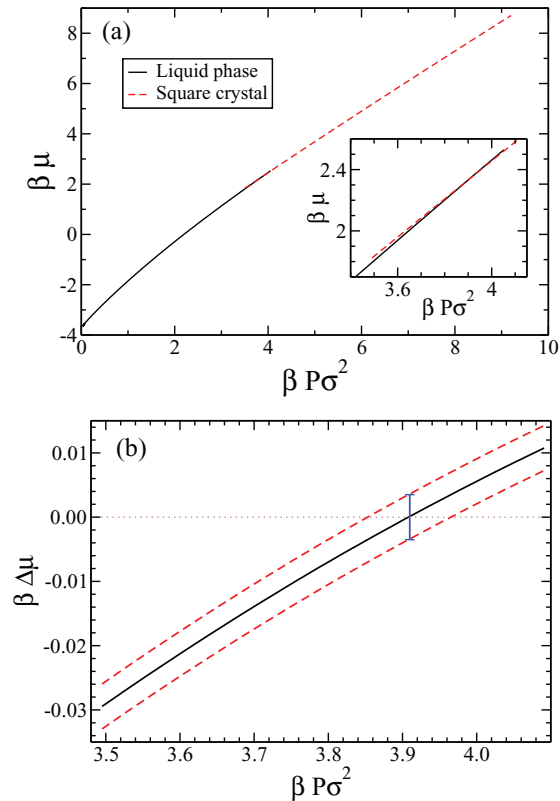


FIG. 5. Determination of a coexistence P between the L and S phases at $k_B T/\epsilon = 0.55$. Panel (a) shows the chemical potential isotherms for the liquid (solid curve) and the square crystal (dashed curve). Inset shows a closeup of the crossing. In panel (b) we show the difference in chemical potential $\Delta\mu$ between the two phases over the entire range of P for which the equations of state overlap, with dashed lines indicating upper and lower uncertainty estimates.

which is equal to

$$\beta f_{\text{Ein}} = \frac{\beta U(\vec{r}_0^N)}{N} - \frac{d}{2} \ln\left(\frac{\pi}{\beta \lambda_{\text{max}}}\right), \quad (9)$$

where $U(\vec{r}_0^N)$ is the potential energy of the crystal when all the atoms are at their ideal lattice positions, and λ_{max} is chosen such that, for λ larger than λ_{max} , the mean-squared displacement $\langle \delta r^2 \rangle_\lambda \equiv \langle (\vec{r}_i - \vec{r}_{0,i})^2 \rangle_\lambda$, where $\langle \dots \rangle_\lambda$ indicates an ensemble average, for a system with fixed center of mass follows the following analytical expression:

$$\langle \delta r^2 \rangle_{\text{Eins}, \lambda} = \frac{N-1}{N} \frac{1}{\beta \lambda}. \quad (10)$$

The second term in Eq. (8) represents the free energy difference between the solid and the Einstein crystal, and can be calculated by integrating the mean-squared displacement obtained from simulations carried out with a fixed center of mass as follows:^{40,49}

$$\frac{\Delta F^{\text{CM}}}{N} = \int_0^{\lambda_{\text{max}}} \langle \delta r^2 \rangle_\lambda d\lambda. \quad (11)$$

This integration can be understood as gradually switching on the coupling parameter to transform the solid into an Einstein crystal. For better accuracy, this integral can be transformed to⁴⁰

$$\frac{\Delta F^{\text{CM}}}{N} = \int_{\ln(c)}^{\ln(\lambda_{\text{max}}+c)} d[\ln(\lambda+c)] (\lambda+c) \langle \delta r^2 \rangle_\lambda, \quad (12)$$

where c is a constant chosen to be 1 in this work. The integrand is shown in Fig. 4, along with the curve for the ideal solid. We choose $\ln(\lambda_{\text{max}} + 1) = 6.909$, checking that using higher values yields no appreciable change in the final result. The integration is carried out using interpolations of different order in order to estimate uncertainty.

The third, fourth, and fifth terms in Eq. (8) correspond to the difference between the constrained (fixed center of mass) and unconstrained (non-fixed center of mass) solids. The last term in Eq. (8) is the free energy of the ideal gas per particle, which is given by

$$\beta f_{\text{id}} = \ln(\rho) - 1 + \frac{\ln(2\pi N)}{2N}. \quad (13)$$

Once the chemical potentials of the two phases are known, the coexistence point can be obtained from the intersection of the two chemical potential curves.^{46,47}

$\mu_l(\rho)$ and $\mu_s(\rho)$ are used together with the equations of state to plot the chemical potentials of the two phases as functions of pressure, as we do in Fig. 5. It is immediately apparent that $\mu(P)$ has nearly the same slope for both phases, and hence the location of the crossing is sensitive to errors in the various calculated quantities used to determine the curves. We note that the equations of state are determined only to the point where the metastable phase does not easily transform to the other phase. It is somewhat surprising that at the P for which either phase becomes unstable, $\beta P \sigma^2 \sim 3.49$ for S and $\beta P \sigma^2 \sim 4.09$ for L, the difference in chemical potential is very small, on the order of $|\beta \Delta \mu| \sim 0.01$.

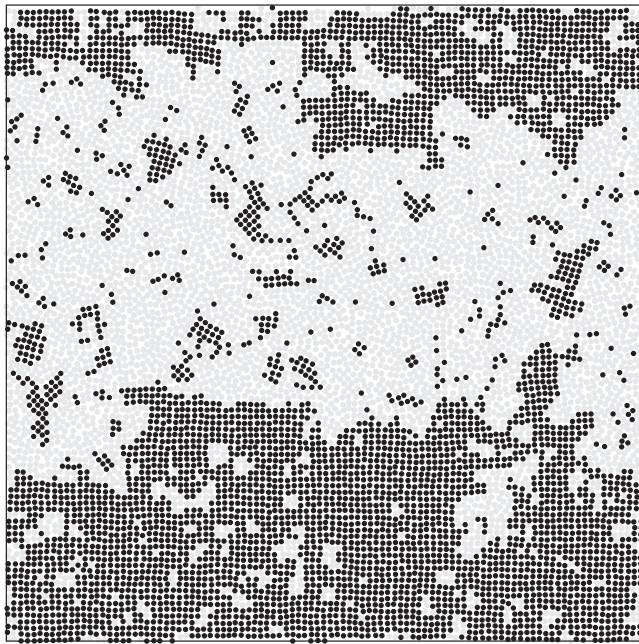


FIG. 6. Snapshot configuration obtained from an NVT simulation for 10 000 particles at $k_B T/\epsilon = 0.55$ and $\rho = 0.786567$. Black symbols represent particles belonging to the S phase, while grey symbols represent the L phase.

As a check on the L-S coexistence conditions at $k_B T/\epsilon = 0.55$, we perform an NVT (canonical ensemble) simulation with 10 000 particles initially placed on a square lattice with $\rho\sigma^2 = 0.786567$, the ρ at which the system is expected to phase separate into L and S with equal numbers of particles in each phase, based on liquid and S coexistence densities of $\rho_l = 0.7677$ and $\rho_x = 0.8064$, respectively. Figure 6 shows a snapshot after running for 2×10^7 MC steps per particle, with dark symbols identifying particles belonging to the S phase.^{50–53} Averaging over the last 5×10^6 MC steps per particle, the fraction of particles belonging to the S phase is 0.51.

The above procedure is repeated (at lower T) for the other crystal phases to determine crystal-crystal coexistence lines. For two crystals, the slopes of $\mu(P)$ are generally quite different, which makes it easier to pinpoint the coexistence P . Similarly, at T less than the L-G critical temperature, the procedure is repeated to find crystal sublimation lines after determining the equation of state for the gas.

For the L-LDT melting line, we must additionally perform an integration of the enthalpy H to lower T at a P above the critical pressure in order to avoid the L-G critical point. Specifically, we first integrate the liquid equation of state at $k_B T/\epsilon = 0.70$ using Eq. (2) to $P\sigma^2/\epsilon = 0.05$, and then calculate $\mu(T)$ via⁴⁹

$$\frac{\mu(T_2, P)}{k_B T_2} = \frac{\mu(T_1, P)}{k_B T_1} - \int_{T_1}^{T_2} \frac{H(T)}{N k_B T^2} dT, \quad (14)$$

noting that here, the T dependence of Λ must be taken into account. Equivalently, this amounts to using the potential energy instead of the thermal energy in calculating H . For the LDT crystal, the reference free energy is calculated at $P\sigma^2/\epsilon = 0.05$ and $k_B T/\epsilon = 0.24$ after determining the density at that point to be $\rho\sigma^2 = 0.4780 \pm 0.0015$. In Fig. 7

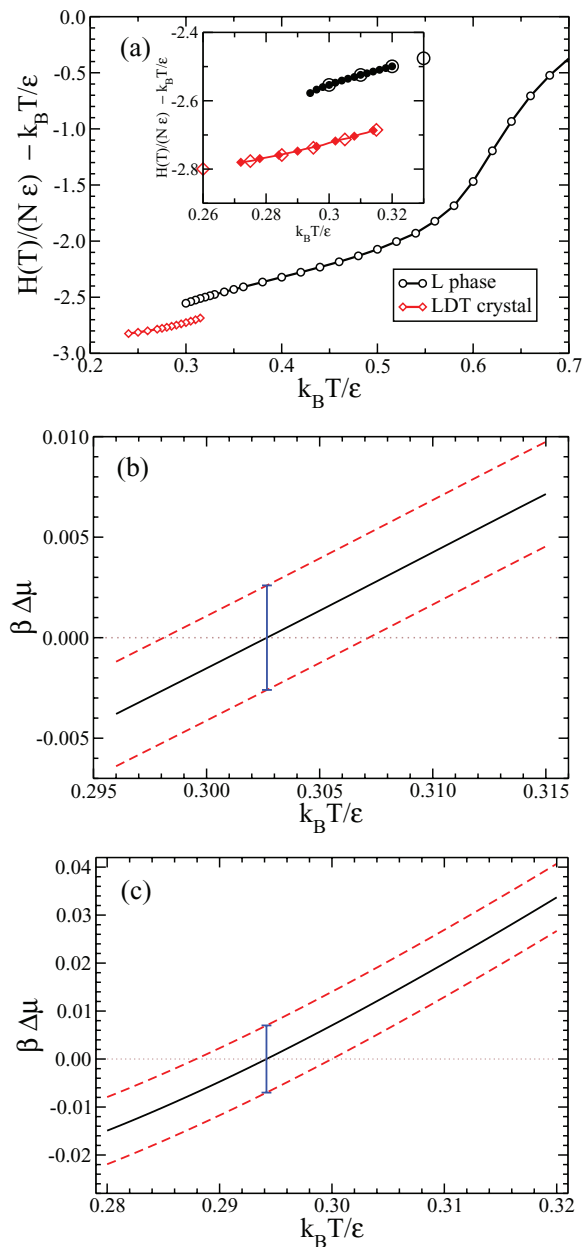


FIG. 7. (a) Enthalpy per particle for the liquid (circles) and LDT crystal (diamonds) along $P\sigma^2/\epsilon = 0.05$. Here we have subtracted the ideal gas contribution to the energy. Inset shows data for a larger system of approximately 4000 particles (filled symbols). (b) The corresponding chemical potential difference between the L and LDT phases for the entire range in T of metastability. (c) The chemical potential difference between the L and S phases at $P\sigma^2/\epsilon = 0.15$.

show $H(T)$ for L and LDT as well as the resulting difference in μ between the phases. We repeat the calculation using the liquid equation of state at $k_B T/\epsilon = 0.55$ as a check. Using the same procedure at $k_B T/\epsilon = 0.70$, we carry out an evaluation of the melting temperature of the S phase at $P\sigma^2/\epsilon = 0.15$ [Fig. 7(c)] and $P\sigma^2/\epsilon = 7.00$ as a check on the accuracy of the coexistence line. In the inset of Fig. 7(a), we plot H for L and LDT for a larger system of ~ 4000 particles, detecting no appreciable difference in the value of H per particle or range of metastability from the ~ 1000 particle system. We similarly

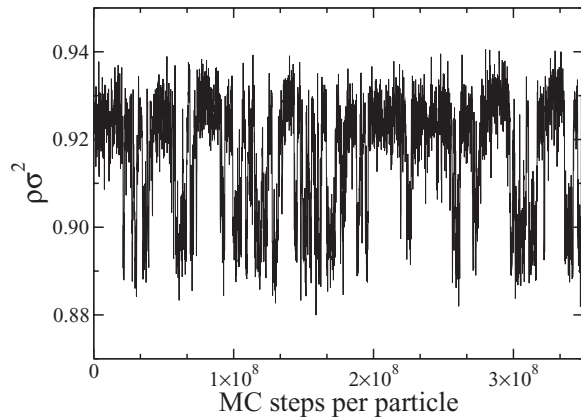


FIG. 8. Sample time series of the number density near the L-HDT coexistence curve, with $N = 986$, $k_B T/\epsilon = 5.0$, and $P_0 = 50.0\epsilon/\sigma^2$. The system samples both the (lower density) liquid and the HDT crystal.

detect no differences for the L-S transition when increasing the system size to 4000 particles (not shown).

C. L-HDT coexistence

Using the Gibbs-Duhem integration method is not necessary (or possible) for tracing out the L-HDT melting line at high T , as over a certain range in P the system can fairly easily sample both states. Thus, to determine the coexistence P along an isotherm, we first locate a pressure P_0 for which we can sample both states with reasonable statistics, as shown in Fig. 8, and determine the conditional Gibbs free energy from a histogram of the densities sampled during an NPT simulation

$$\beta \Delta G(T, P_0; \rho) = -\ln [P_r(\rho)], \quad (15)$$

where $P_r(\rho)$ is the probability density of observing the system at a particular ρ . Here, we do not normalize our histograms as the normalization merely adds an inconsequential shift. P_0 already provides an estimate of the location of the coexistence pressure. The conditional free energy shown in Fig. 9 (black curve) exhibits a global minimum at high density (HDT) and a metastable one at low density (liquid). The free energy barrier between the two states is characteristic of a first-order transition. To more precisely locate the coexistence pressure, we reweight the histogram by applying a pressure shift,

$$\beta \Delta G(T, P'; \rho) = \beta \Delta G(T, P_0; \rho) + \frac{N\beta \Delta P}{\rho} + c, \quad (16)$$

where c is a constant related to normalization and ΔP is the pressure shift that brings the two minima to the same level, as in Fig. 9 (red curve). The coexistence pressure is then equal to $P' = P_0 + \Delta P$. In practice, the shift we obtain is hardly perceptible on the scale of our plots, e.g., for the $k_B T/\epsilon = 5.0$ case in Fig. 9, $P_0 \sigma^2/\epsilon = 50.0$ and $\Delta P \sigma^2/\epsilon = -0.135$, and for $k_B T/\epsilon = 1.0$, $P_0 \sigma^2/\epsilon = 14.350$ and $\Delta P \sigma^2/\epsilon = -0.004$. We note that the barrier does grow with decreasing T , and below $k_B T/\epsilon \approx 0.5$, both phases can stably exist for sufficiently long times in order to perform the Gibbs-Duhem integration. Indeed below this T , it is not feasible to continue with histogram reweighting without using some biasing potential within the MC simulations.

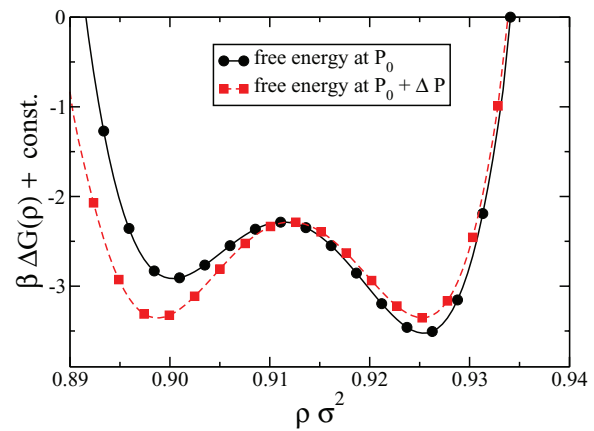


FIG. 9. Conditional Gibbs free energy as a function of ρ . At $k_B T/\epsilon = 5.0$ and a pressure $P_0 = 50.0\epsilon/\sigma^2$ slightly above coexistence (solid curve, circles), the high-density basin (HDT crystal) has a lower free energy than the low-density (liquid) basin. Through Eq. (16), an appropriate shift in the pressure locates the coexistence pressure, i.e., transforms the P_0 curve so that the liquid and HDT minima are at the same level to within precision of the data (dashed line, squares).

D. G-L coexistence

The G-L coexistence line can be determined by using the Gibbs ensemble MC method developed by Panagiotopoulos.⁵⁴ The Gibbs ensemble employs two separated subsystems (without the presence of an interface), where the total number of particles is fixed and the total volume (in this case, area) of the two subsystems is also fixed; the total system as a whole evolves according to the canonical ensemble. The thermodynamic requirements for phase coexistence are that the temperature, pressure, and chemical potential of the two coexisting phases must be equal and these requirements can be achieved by performing three different kinds of trial MC moves. First, particle displacement within each subsystem, second, volume fluctuations of the two subsystems, and third, transferring particles between the two subsystems. The advantage of using the Gibbs ensemble is that the system finds the densities of the coexistence phases without computing either the pressure or the chemical potential.

Having obtained the coexistence densities at a series of T , the corresponding coexistence pressures can be estimated by applying the virtual volume change method of Haresmiadis *et al.*⁵⁵ In this method, we perform separate NVT MC simulations of both the liquid and the gas at their respective coexistence densities (at a given T), and obtain the pressure via

$$P = \frac{k_B T}{\Delta V} \ln \left[\left\langle \left(\frac{V'}{V} \right)^N \exp(-\beta \Delta U) \right\rangle \right], \quad (17)$$

where ΔU is the potential energy difference between a configuration with particle coordinates isotropically rescaled to accommodate a smaller virtual area V' and the unaltered configuration with original area V , where $V' = V - \Delta V$ and $\Delta V = 0.1\sigma^2$. Both phases give the same pressure to within error.

However, as the temperature approaches the critical temperature T_C , G-L coexistence can no longer be discerned in

the Gibbs ensemble simulation. Our data for the G-L coexistence curve from the Gibbs ensemble extend only to $k_B T/\epsilon = 0.50$. Beyond this T , we extrapolate according to the following procedure. We estimate T_C by fitting the density difference of the two coexisting phases to a scaling law^{40,46,56}

$$\rho_l - \rho_g = A|T - T_C|^{\beta_c}, \quad (18)$$

where β_c is the critical exponent, which is equal to 0.125 for a two-dimensional system, and A is a constant determined from the fit. To estimate the critical density ρ_C , we fit our results to the law of rectilinear diameters^{40,46,56}

$$\frac{\rho_l + \rho_g}{2} = \rho_C + B|T - T_C|, \quad (19)$$

where B is a constant determined in the fit, and T_C is used from the fit in Eq. (18). The critical pressure P_C is estimated by fitting the vapor pressure curve to the Clausius-Clapeyron equation⁵⁶

$$\ln P = C + \frac{D}{T}, \quad (20)$$

where C and D are constants determined in the fit. P_C is then calculated by substituting T_C obtained from Eq. (18) in Eq. (20). From the fits, we obtain $\rho_C \sigma^2 = 0.263 \pm 0.002$, $k_B T_C/\epsilon = 0.533 \pm 0.002$, and $P_C \sigma^2/\epsilon = 0.019 \pm 0.001$. The uncertainties quoted here are based on uncertainties in the fit parameters and do not reflect any systematic error associated with the fact that we are extrapolating above $k_B T/\epsilon = 0.50$, the highest T at which we have reliable Gibbs ensemble data.

III. RESULTS

Having assembled all of the individual coexistence curves, we present the phase diagram in the P - T plane in Fig. 10 and in the ρ - T plane in Fig. 11. The three panels of Fig. 10 show progressively smaller ranges of P . In Fig. 10(b), dashed lines indicate metastable extensions of coexistence lines into the gas stability field (i.e., showing the phase diagram in the absence of the gas). As an aid to interpreting Fig. 11, we recall that under conditions of constant volume, the thermodynamic ground state is not necessarily a single phase, but is generally composed of two coexisting phases. The bottom panel of Fig. 11 shows the phase diagram in the absence of the gas phase.

Figure 10(a) shows a prominent S-L melting line temperature maximum at $P\sigma^2/\epsilon = 5.24 \pm 0.05$ and $k_B T_{\max}/\epsilon = 0.655 \pm 0.005$. At this point, according to Eq. (1), the molar volumes of the S crystal and liquid are equal. At higher P , the melt is more dense than the crystal, as in the familiar case of water and hexagonal ice.

An even more exotic feature of the S-L melting line is the pressure maximum occurring near the HDT-S-L triple point at $P_{\max}\sigma^2/\epsilon = 7.98 \pm 0.08$ and $k_B T/\epsilon = 0.450 \pm 0.003$. A closeup of this feature is shown in Fig. 12. At this point, according to Eq. (1), the entropy of the S crystal and the liquid are equal, and for lower T along the curve, the melt has a *lower* entropy than the crystal. The presence of the pressure maximum in the melting curve allows for “inverse melting”⁵⁷ in the

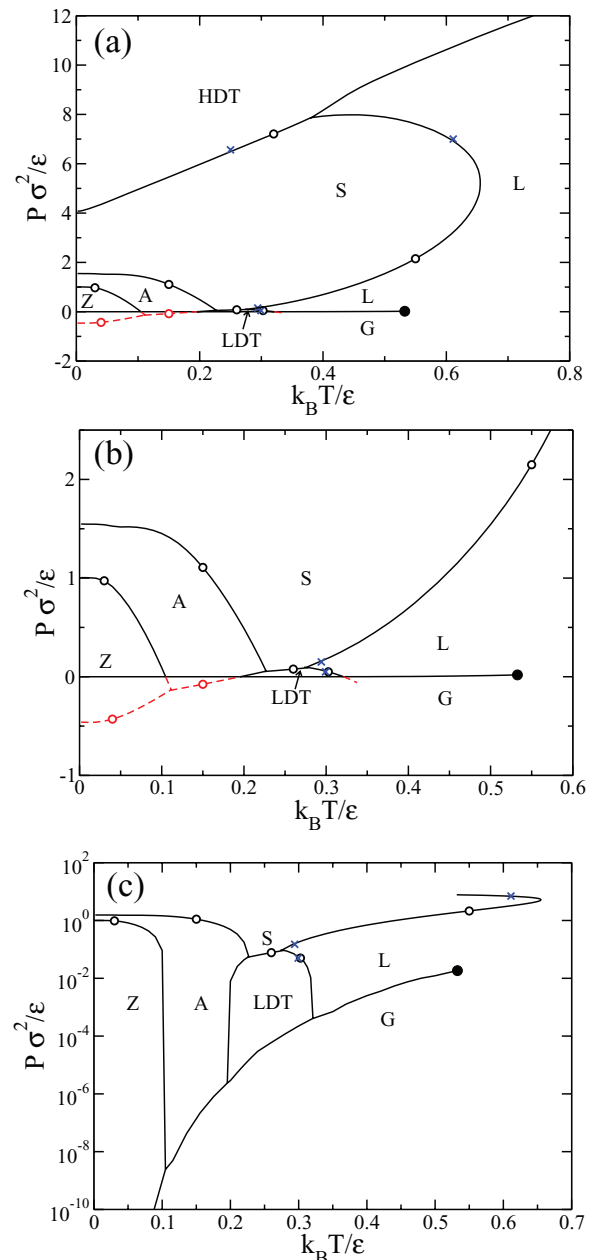


FIG. 10. Phase diagram of the 2D model in the P - T plane, showing the liquid (L), gas (G), and crystal phases HDT, S, LDT, A, and Z (see Fig. 2). The panels show portions of the phase diagram at (a) high, (b) medium, and (c) low P . The liquid-gas coexistence line terminates at a critical point at $k_B T_c/\epsilon = 0.533$ and $P_C \sigma^2/\epsilon = 0.0185$ (filled circle). Dashed lines in (b) are metastable coexistence lines assuming the absence of the gas phase. Initial coexistence points, i.e., starting points for Gibbs-Duhem integration, are indicated by circles, while \times 's show repeated coexistence calculations done as checks on the Gibbs-Duhem integration.

narrow range of P between the triple point and the maximum, i.e., isobaric heating of the liquid results in crystallization.

Given the numerical uncertainties in determining coexistence conditions and tracing out coexistence lines, we carry out a rough check by performing three sets of simulations in the vicinity of the HDT-S-L triple point. Each set is a grid of 121 simulations for state points marked in Fig. 12. For one set, the particles are initially positioned on the S lattice; for the second set, points are initially on the HDT lattice; high

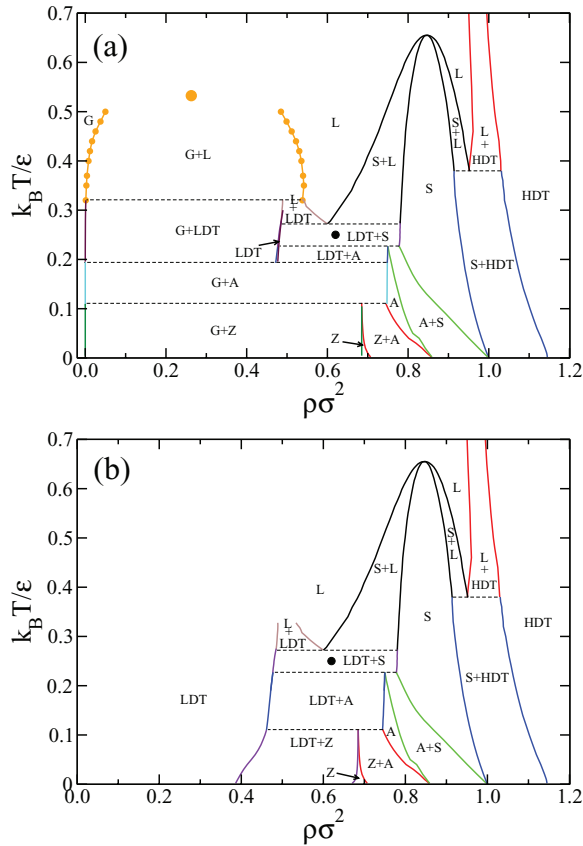


FIG. 11. Phase diagram in the ρ - T plane. (a) The points along the G-L coexistence lines indicate results from Gibbs Ensemble simulations and the large filled orange circle shows our estimate of the G-L critical point based on an extrapolation described in the text. Panel (b) shows the phase diagram in the absence of the gas phase. The filled black circle shows the location of the obscured L-L critical point discussed in Ref. 39.

T liquid-state configurations seed the third set of simulations. We run each simulation for 5×10^7 MC steps per particle, and then indicate with the appropriate symbol in Fig. 12 the phase which the system spontaneously adopts. Potentially,

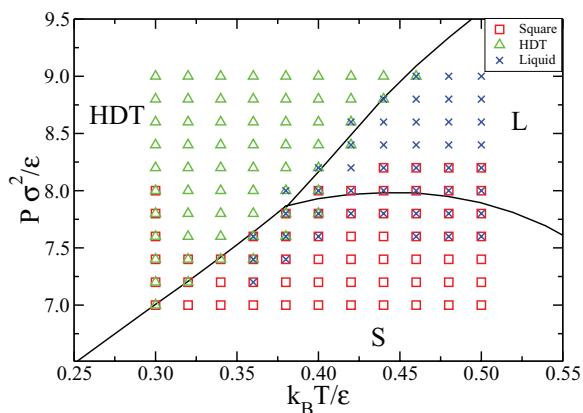


FIG. 12. P- T phase diagram obtained at high pressure, near the L-S-HDT triple point. The grid of points is obtained from three sets of simulations. Each of L, S, and HDT is used to initialize a simulation set with $N = 986$, 992, and 986, respectively. The final phase adopted from each set at each state point is indicated by a symbol: S, square; HDT, triangle; L, \times . For example, at low P and high T , both L and HDT transform to S, while near the triple point, each phase retains metastability.

tially, since there are three simulations per state point, three symbols may appear, indicating stability or metastability of all three phases. Near the triple point, the simulations retain the starting phase, as expected, while deep within a stability field, all sets transform to the same phase. In this way, we crudely map out the extent of metastability.

It is difficult to directly confirm inverse melting on typical simulation time scales, as the metastable phase is never far from the coexistence line. We aim to address this in future work. However, and while this is not a definitive check on the existence of inverse melting, the tendency for points exhibiting liquid metastability within the S stability field to track the curvature of the S-L melting line is supportive of the existence of this phenomenon in the system, i.e., the lowest P point for each T for which the \times and \circ simultaneously occur roughly form a curve with a maximum in P that tracks the shape of the S-L coexistence line.

At lower P , we confirm the negative slope of the LDT-L melting line as reported already in Ref. 39. Below the LDT-S-L triple point, we find that the new crystal phases A and Z both have reasonably large stability fields, as shown in Fig. 10(b), and that the LDT crystal, having the lowest density of the crystal phases studied, occupies a rather small portion of the phase diagram. The A-S transition line is also negatively sloped, which together with the fact that the A phase has a lower density than S (see Fig. 11), implies through Eq. (1) that the entropy of S is larger than that of A. Indeed, the bonding distances required to form A are rather restrictive compared to the geometry of S, and this is reflected in the smaller range in ρ for which A is the single stable phase (again, compared to S). A similar argument holds when comparing Z to A.

The nature of phases A and Z is somewhat reminiscent of the low-density phases appearing in soft shoulder models,^{33,34} in that in both cases the system sacrifices entropy in favor of lower energy at low T by effectively increasing the particle size to the soft diameter. Here, however, the particular low energy bond length allows the system to form particle geometries that progressively lower the energy. That there are several low-density crystals is also reminiscent of water and silica.

In Ref. 39, the authors locate lines in the P - T plane that demarcate a limit to observing the liquid, i.e., where crystallization is practically unavoidable. Although their investigation into this aspect of the model was not exhaustive, the character of crystallization was possibly suggestive of continuous crystallization seen in other two-dimensional systems. We plot these lines within the appropriate portion of our calculated phase diagram in Fig. 13. We see that the crystallization lines occur below our calculated first-order melting lines, and therefore occur at conditions for which there is a gap in crystal and liquid chemical potential. However, this does merit a closer look at the crystallization process, especially near the apparent limit of liquid metastability. Also in Fig. 13, we plot the location of what might be termed the obscured L-L critical point at low T that appears to be responsible for the liquid anomalies reported in Ref. 39, but which is unobservable owing to unavoidable nucleation. Within uncertainty, this obscured critical point falls on the S-LDT coexistence line.

We estimate the density of the obscured critical point from the pressure isochores reported in Ref. 39, and plot the

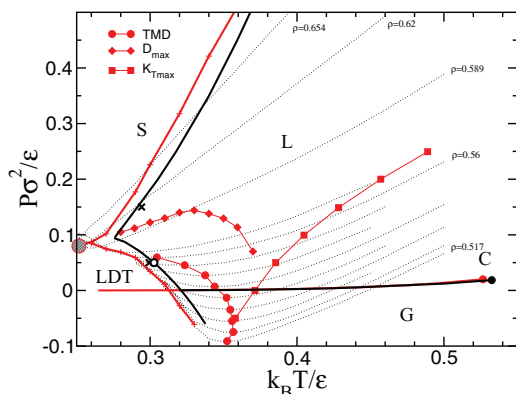


FIG. 13. Comparison of our phase diagram with previously reported system properties. Red curves are taken from Ref. 39 and represent crystallization lines (+), locus of temperatures of maximum density along isobars (TMD, circles), pressures of maximum diffusivity along isotherms (D_{\max} , diamonds), maxima of isothermal compressibility ($K_{T\max}$, squares), and G-L coexistence. Also shown are the G-L critical point (filled red circle) and the obscured L-L critical point (large hashed circle). Dotted lines show pressure along isochores. All other symbols as in Fig. 10. We note that we determine the location of the G-L critical point from an extrapolation of data above $k_B T/\epsilon = 0.50$, while the one reported in Ref. 39 is based on inflection points of pressure isotherms. The previously reported crystallization lines fall within the presently calculated crystal stability fields.

location in the ρ - T plane in Fig. 11. We see that it falls within the coexistence region of two crystals (S and LDT) of significantly different ρ . This is similar to the case of, e.g., the TIP4P2005 model of water^{58,59} and is consistent with the idea that L-L phase separation is possible when there is a strong coupling between energy and density.⁶⁰

IV. DISCUSSION

We calculate the coexistence temperature (along an isobar) or pressure (along an isotherm) of two phases by determining the point at which the chemical potential of those two phases cross, and estimate the uncertainty by accounting for the numerical error, typically arising from an integration, in evaluating the various terms in, e.g., Eqs. (2), (12) and (14). The errors mostly result in a constant shift in the curves that, given the small difference in slopes of $\mu(P)$ or $\mu(T)$ between the liquid and crystal phases, can lead to a large uncertainty in the crossing. As a check, after calculating the coexistence curve through the Gibbs-Duhem integration, for the L-S case, for example, we determine two additional chemical potential crossings along different thermodynamic paths and the results show good consistency with the Gibbs-Duhem curve. Another indicator of the quality of the results is the degree to which coexistence lines cross at the L-S-HDT and L-S-LDT triple points.

Having said this, shifts in the $\mu(P)$ or $\mu(T)$ curves do not affect the slopes, which show in general the first-order character of the L-S or L-LDT transitions. For a given phase, we determine μ to the point where it is simple to determine the equilibrium properties of that phase, i.e., to the point where spontaneous transformation does not readily occur on the timescale of simulation. We note that for the liquid to crystal transitions, the chemical potential difference between the

liquid and crystal at which metastability is no longer easily attainable is rather small in comparison to other studies.⁶¹ Perhaps this is a feature of two-dimensional systems, but nonetheless implies a very small surface tension if the classical description of nucleation is valid.

The L-LDT and L-S crystallization lines in Ref. 39, as noted earlier, were dynamically determined as maximal extents of the liquid's ability to exist, and we show here that they indeed occur in the metastable liquid. The loss of liquid metastability prevents observing any low- and high-density liquids that would exist below the proposed L-L critical point because these limit lines radiate from the critical point towards higher T . We would like to explore the process of crystallization in this vicinity. If indeed the L-L critical point proposed for this system is obscured by nucleation induced through critical fluctuations, studying nucleation in the present model may help better understanding what may be occurring in water.⁶²

Notably, for the model at higher P , we provide evidence for inverse melting, arising from a maximum in P in the L-S coexistence line. This phenomenon is rare, and seeing evidence for it in such a simple system will allow for deeper exploration into the basic physics surrounding it.

The freezing of the liquid to the close-packed solid, i.e., the L-HDT transition, appears to be first order for all T that we have explored. For our system size, the free energy barrier between the L and HDT basins with ρ as the order parameter at $k_B T/\epsilon = 5.0$ and $P = 50.0\epsilon/\sigma^2$ is just above $1k_B T$. In the high T limit when the system should behave as hard disks, Mak⁶³ and Bernard and Krauth⁶⁴ have provided evidence that the transition should be also first order. Lowering T , the barrier grows and reaches a value of $\sim 2.4k_B T$ at a simulation conducted on our coexistence line at $k_B T/\epsilon = 0.50$ and $P\sigma^2/\epsilon = 9.5649$ with $N = 986$, thus becoming more strongly first order. A careful search for the hexatic phase near the HDT melting line is very much warranted, particularly at high T , as Bernard and Krauth's rather impressive work appears to establish a first-order transition between the liquid and hexatic (not crystal) phase in hard disks, and that the hexatic phase exists only for a very narrow range of densities. Our initial search for the hexatic phase through discrete molecular dynamics simulations at constant P of 65 536 particles for $k_B T/\epsilon \leq 5.0$ along the HDT melting line as well as at points near the L-S and L-LDT transition lines has not yet yielded evidence for the hexatic phase, namely, an orientational correlation function that decays with distance as a power law with a sufficiently small exponent.⁶⁵ It would seem then, that if it exists, the presence of the hexatic phase would not affect our phase diagram in a significant way. Interestingly, Bernard and Krauth did not establish a power-law decay of the orientational correlation function within the hexatic phase. We hope to report on this more thoroughly in the future.

V. CONCLUSIONS

We compute a phase diagram using various free energy techniques of a two-dimensional SSSW model that has been previously shown to exhibit liquid-state anomalies often associated with the presence of a metastable L-L critical point.¹⁸

We find two low- T crystal phases not previously reported. All transitions, including melting lines, appear to be first order for our system size of ~ 1000 particles. Thus, it appears that the liquid anomalies present in the system do not arise as a result of quasi-continuous freezing, as has been previously suggested.⁶⁶ Previously reported crystallization lines fall within respective phase stability regions reported here. Interestingly, the difference in chemical potential between liquid and crystal phases at the limit where the metastable phase can be readily observed is rather small, $\beta\Delta\mu \sim 0.01$.

The L-S coexistence curve exhibits both a maximum temperature, indicating that at higher pressure the crystal is less dense than the melt, and a pressure maximum, which means that inverse melting should occur in a specific pressure range. Given the scarcity of systems exhibiting inverse melting, the present model presents the opportunity to study this rare phenomenon in more detail.

ACKNOWLEDGMENTS

A.M.A. and I.S.-V. thank Natural Sciences and Engineering Research Council (Canada) (NSERC) for funding, the Atlantic Computational Excellence Network (ACEnet) for funding and computational support, and Canada Foundation for Innovation (CFI) for funding of computing infrastructure. S.V.B. acknowledges the partial support of this research through the Dr. Bernard W. Gamson Computational Science Center at Yeshiva College.

¹P. C. Hemmer and G. Stell, *Phys. Rev. Lett.* **24**, 1284 (1970).

²G. Stell and P. C. Hemmer, *J. Chem. Phys.* **56**, 4274 (1972).

³J. S. Hoye and P. C. Hemmer, *Phys. Norv.* **7**, 1 (1973).

⁴K. K. Mon, N. W. Ashcroft, and G. V. Chester, *Phys. Rev. B* **19**, 5103 (1979).

⁵M. Selbert and W. H. Young, *Phys. Lett. A* **58**, 469 (1976).

⁶D. Levesque and J. J. Weis, *Phys. Lett. A* **60**, 473 (1977).

⁷J. M. Kincaid and G. Stell, *Phys. Lett. A* **65**, 131 (1978).

⁸P. T. Cummings and G. Stell, *Mol. Phys.* **43**, 1267 (1981).

⁹A. Voronel, I. Paperno, S. Rabinovich, and E. Lapina, *Phys. Rev. Lett.* **50**, 247 (1983).

¹⁰K. K. Mon, N. W. Ashcroft, and G. V. Chester, *J. Phys. F* **15**, 1215 (1985).

¹¹E. Velasco, L. Mederos, G. Navascues, P. C. Hemmer, and G. Stell, *Phys. Rev. Lett.* **85**, 122 (2000).

¹²C. H. Cho, S. Singh, and G. W. Robinson, *Phys. Rev. Lett.* **76**, 1651 (1996).

¹³M. R. Sadr-Lahijany, A. Scala, S. V. Buldyrev, and H. E. Stanley, *Phys. Rev. Lett.* **81**, 4895 (1998).

¹⁴M. R. Sadr-Lahijany, A. Scala, S. V. Buldyrev, and H. E. Stanley, *Phys. Rev. E* **60**, 6714 (1999).

¹⁵E. A. Jagla, *J. Chem. Phys.* **111**, 8980 (1999).

¹⁶E. A. Jagla, *Phys. Rev. E* **63**, 061501 (2001).

¹⁷E. A. Jagla, *Phys. Rev. E* **63**, 061509 (2001).

¹⁸A. Scala, M. R. Sadr-Lahijany, N. Giovambattista, S. V. Buldyrev, and H. E. Stanley, *Phys. Rev. E* **63**, 041202 (2001).

¹⁹T. Head-Gordon and F. H. Stillinger, *J. Chem. Phys.* **98**, 3313 (1993).

²⁰F. H. Stillinger and T. Head-Gordon, *Phys. Rev. E* **47**, 2484 (1993).

²¹P. H. Poole, F. Sciortino, U. Essmann, and H. E. Stanley, *Nature (London)* **360**, 324 (1992).

²²E. Rapoport, *J. Chem. Phys.* **46**, 2891 (1967).

²³V. V. Brazhkin, S. V. Popova, and R. N. Voloshin, *High Press. Res.* **15**, 267 (1997).

²⁴M. J. Cuthbertson and P. H. Poole, *Phys. Rev. Lett.* **106**, 115706 (2011).

²⁵V. V. Vasishat, S. Saw, and S. Sastry, *Nat. Phys.* **7**, 549 (2011).

²⁶J. N. Glosli and F. H. Ree, *Phys. Rev. Lett.* **82**, 4659 (1999).

²⁷G. Franzese, G. Malescio, A. Skibinsky, S. V. Buldyrev, and H. E. Stanley, *Nature (London)* **409**, 692 (2001).

²⁸S. V. Buldyrev, G. Malescio, C. A. Angell, N. Giovambattista, S. Prestipino, F. Saija, H. E. Stanley, and L. Xu, *J. Phys.: Condens. Matter* **21**, 504106 (2009).

²⁹U. Gasser, *J. Phys.: Condens. Matter* **21**, 203101 (2003).

³⁰P. J. Camp, *Phys. Rev. E* **68**, 061506 (2003).

³¹H. M. Gibson and N. B. Wilding, *Phys. Rev. E* **73**, 061507 (2006).

³²V. N. Ryzhov and S. M. Stishov, *Phys. Rev. E* **67**, 010201(R) (2003).

³³Y. D. Fomin, N. V. Gribova, V. N. Ryzhov, S. M. Stishov, and D. Frenkel, *J. Chem. Phys.* **129**, 064512 (2008).

³⁴N. V. Gribova, Y. D. Fomin, D. Frenkel, and V. N. Ryzhov, *Phys. Rev. E* **79**, 051202 (2009).

³⁵C. J. Roberts and P. G. Debenedetti, *J. Chem. Phys.* **105**, 658 (1996).

³⁶C. Buzano and M. Pretti, *J. Chem. Phys.* **119**, 3791 (2003).

³⁷C. Buzano, E. De Stefanis, and M. Pretti, *J. Chem. Phys.* **129**, 024506 (2008).

³⁸N. G. Almarza, J. A. Capitán, J. A. Cuesta, and E. Lomba, *J. Chem. Phys.* **131**, 124506 (2009).

³⁹S. V. Buldyrev, G. Franzese, N. Giovambattista, G. Malescio, M. R. Sadr-Lahijany, A. Scala, A. Skibinsky, and H. E. Stanley, *Physica A* **304**, 23 (2002).

⁴⁰Daan Frenkel and Berend Smit, *Understanding Molecular Simulation: From Algorithms to Applications* (Academic Press, San Diego, 2002).

⁴¹D. A. Kofke, *Mol. Phys.* **78**, 1331 (1993).

⁴²D. A. Kofke, *J. Chem. Phys.* **98**, 4149 (1993).

⁴³M. H. Lamm and C. K. Hall, *AIChE J.* **50**, 215 (2004).

⁴⁴The algorithm used is $P_{i+1} = P_i + \Delta T(f_i + f_{i+1})/2$, where f_i is the right hand side of Eq. (1), the evaluation of which requires one NPT MC simulation for each phase at temperature T_i and pressure P_i . Alternatively, we iterate $T_{i+1} = T_i + \Delta P(1/f_i + 1/f_{i+1})/2$. This is especially useful in the vicinity of the melting temperature maximum of the S-L coexistence curve.

⁴⁵C. Vega and E. G. Noya, *J. Chem. Phys.* **127**, 154113 (2007).

⁴⁶M. G. Noro and D. Frenkel, *J. Chem. Phys.* **114**, 2477 (2001).

⁴⁷D. L. Pagan and J. D. Gunton, *J. Chem. Phys.* **122**, 184515 (2005).

⁴⁸D. Frenkel and A. J. C. Ladd, *J. Chem. Phys.* **81**, 3188 (1984).

⁴⁹C. Vega, E. Sanz, J. L. F. Abascal, and E. G. Noya, *J. Phys.: Condens. Matter* **20**, 153101 (2008).

⁵⁰P. R. ten Wolde, M. J. Ruiz-Montero, and D. Frenkel, *J. Chem. Phys.* **104**, 9932 (1996).

⁵¹A. M. Al mudallal and I. Saika-Voivod, *Phys. Rev. E* **84**, 011402 (2011).

⁵²I. Saika-Voivod, P. H. Poole, and R. K. Bowles, *J. Chem. Phys.* **124**, 224709 (2006).

⁵³The solid particles have been identified using the method developed by Frenkel and co-workers (Ref. 50). For each particle we define the quantity $q_{lm}(i) = 1/N_b(i) \sum_{j=1}^{N_b(i)} Y_{lm}(\hat{r}_{ij})$, where the sum is carried out over all neighboring particles $N_b(i)$ that are within a distance $\sqrt{2}a$, and $Y_{lm}(\hat{r}_{ij})$ are the spherical harmonics calculated for the normalized direction vector \hat{r}_{ij} between the neighbors. The unit vector \hat{r}_{ij} is determined by the polar and azimuthal angles $\theta_{ij} \equiv \pi/2$ and ϕ_{ij} . Since our crystallites possess square symmetry, we use $l = 4$. For each pair of neighboring particles i and j , we calculate the correlation $\sum_{m=-4}^4 \hat{q}_{4m}(i) \hat{q}_{4m}^*(j)$, where $\hat{q}_{4m} = q_{4m}(i) / [\sum_{m=-4}^4 q_{4m}(i)^2]^{1/2}$ and q^* is the complex conjugate of q . If the correlation between two neighboring particles is greater than 0.9, then particles i and j are considered to be connected. If a particle has at least three connected neighbors, then it is considered a solid particle.

⁵⁴A. Z. Panagiotopoulos, *Mol. Phys.* **61**, 813 (1987).

⁵⁵V. I. Harismiadis, J. Vorholz, and A. Z. Panagiotopoulos, *J. Chem. Phys.* **105**, 8469 (1996).

⁵⁶L. Vega, E. de Miguel, L. F. Rull, G. Jackson, and I. A. McLure, *J. Chem. Phys.* **96**, 2296 (1992).

⁵⁷F. H. Stillinger and P. G. Debenedetti, *Biophys. Chem.* **105**, 211 (2003).

⁵⁸J. L. F. Abascal, E. Sanz, and C. Vega, *Phys. Chem. Chem. Phys.* **11**, 556 (2009).

⁵⁹J. L. F. Abascal and C. Vega, *J. Chem. Phys.* **133**, 234502 (2010).

⁶⁰F. Sciortino, I. Saika-Voivod, and P. H. Poole, *Phys. Chem. Chem. Phys.* **13**, 19759 (2011).

⁶¹I. Saika-Voivod, F. Romano, and F. Sciortino, *J. Chem. Phys.* **135**, 124506 (2011).

⁶²E. B. Moore and V. Molinero, *Nature (London)* **479**, 506 (2011).

⁶³C. H. Mak, *Phys. Rev. E* **73**, 065104(R) (2006).

⁶⁴E. P. Bernard and W. Krauth, *Phys. Rev. Lett.* **107**, 155704 (2011).

⁶⁵P. Keim, G. Maret, and H. H. von Grünberg, *Phys. Rev. E* **75**, 031402 (2007).

⁶⁶N. B. Wilding and J. E. Magee, *Phys. Rev. E* **66**, 031509 (2002).